PHYSICAL REVIEW B **93**, 140407(R) (2016)

Spin dynamics and two-dimensional correlations in the fcc antiferromagnetic Sr_2YRuO_6

S. M. Disseler,[1] J. W. Lynn,[1] R. F. Jardim,[2] M. S. Torikachvili,[3] and E. Granado[4]
[1]*NIST Center for Neutron Research, National Institute of Standards and Technology, Gaithersburg, Maryland 20899, USA*
[2]*Instituto de Física, Universidade de São Paulo, CP 66318, São Paulo 05315-970, Brazil*
[3]*Department of Physics, San Diego State University, San Diego, California 92182, USA*
[4]*Institute of Physics "Gleb Wataghin," University of Campinas–UNICAMP, Campinas, São Paulo 13083-859, Brazil*
(Received 30 November 2015; published 15 April 2016)

The face-centered-cubic (fcc) lattice of Ru^{5+} spins in the double perovskite Sr_2YRuO_6 shows a delicate, three-dimensional antiferromagnetic (AFM) ground state composed of stacked square AFM layers. Inelastic neutron scattering data taken on this state reveal a gapped low-energy excitation band emerging from [001] with spin excitations extending to 8 meV. These magnetic excitations are modeled by a simple J_1-J_2 interaction scheme allowing quantitative comparisons with similar materials. At higher temperatures, the low-energy excitation spectrum is dominated by a quasielastic component associated with size fluctuations of two-dimensional AFM clusters that exhibit asymmetric correlations even at low temperatures. Thus, the fcc lattice in general and the double-perovskite structure in particular emerge as hosts of both two-dimensional and three-dimensional dynamics resulting from frustration.

DOI: 10.1103/PhysRevB.93.140407

The large number of competing ground states in geometrically frustrated magnets tends to destabilize the magnetic ordering and may lead to remarkable correlated states at sufficiently low temperatures [1]. An interesting and classical example of a frustrated magnetic geometry is the face-centered-cubic (fcc) lattice with a dominant nearest-neighbor antiferromagnetic (AFM) interaction [2–4]. This lattice, found in many double-perovskite [5] and spinel [6] compounds, shows a dense population of spin tetrahedra, with triangular faces where the spin interactions cannot be simultaneously satisfied. The presence of anisotropy terms or further-neighbor interactions in the spin Hamiltonian tends to stabilize nearly collinear long-range magnetic structures composed of stacked AFM square layers, where the details of the stacking depend on higher-order terms [7–9].

The ordered double-perovskite structure with the general composition $A_2BB'O_6$ where $A =$ Ca, Sr, Ba, is a rich and versatile template for exploring frustrated phenomena on the fcc lattice. Here, the transition metal B and B' sites form interpenetrating fcc lattices and are amenable to a variety of chemical compositions [5] as both sites have octahedral oxygen coordination. A prototypical quasi-fcc lattice of classical spins is Sr_2YRuO_6 (SYRO), which crystallizes in a quasicubic $P2_1/n$ structure with only the Ru^{5+} ions being magnetic in the system ($S = 3/2, L = 0$) [10–13]. This material shows two magnetic transitions, at $T_{N2} \sim 24$ and $T_{N1} \sim 32$ K [11,14–16]. At sufficiently low temperatures ($T < T_{N2}$), the spins order in the type-I AFM structure [10,11] [see Fig. 1(a)], similar to many d^3 and d^5 double perovskites [5,17–21]. For $T_{N2} < T < T_{N1}$, a partially ordered state is observed, with long-range ordered alternating layers coexisting with layers with short-range correlated spins [11]. Finally, above T_{N1}, a magnetically correlated state is observed, with significant correlations up to ∼300 K [11,22]. A second magnetic structure has been recently reported to occur between T_{N1} and T_{N2} [23], however, no evidence of this state was observed in our previous neutron diffraction study [11].

Related A_2YRuO_6 compounds with the $Fm\bar{3}m$ cubic space group such as Ba_2YRuO_6 (BYRO) exhibit a similar phenomenology to SYRO, including type-I AFM structure, double magnetic transitions [24,25], and short-range order at high temperatures [26], while compounds with large monoclinic distortion such as La_2NaRuO_6 order with incommensurate magnetic structures, if at all [5,27–29]. Detailed studies of the spin-excitation spectrum of intermediate compounds such as SYRO are therefore necessary to determine the general nature of the spin dynamics in this class of materials and to what extent spin-orbit effects play a significant role in the emergent dynamics and ground state.

The 13 g ceramic sample in this work is the same sample employed in a previous study and was synthesized by a solid-state reaction [11]. Neutron scattering experiments were performed on the time-of-flight Disk Chopper Spectrometer (DCS) at NIST Center for Neutron Research (NCNR) with neutrons of incident energy $E_i = 9.73$ or 4.64 meV, yielding Gaussian instrumental energy resolutions of 0.5 and 0.15 meV full widths at half maximum at the elastic position, respectively. Additional measurements to higher energies were performed on the BT-7 triple-axis spectrometer at the NCNR [30] employing the horizontally focusing analyzer geometry with a fixed final energy $E_f = 14.7$ meV.

Figures 1(b)–1(i) show neutron scattering intensity plots as a function of the magnitude of the momentum transfer, or wave vector Q, and excitation energies of SYRO at 5, 15, 22, 27.5, 35, 50, 100, and 300 K taken with an incident neutron energy $E_i = 9.73$ meV. In the elastic sector (bottom of each figure), three reflections are observed in the selected Q interval at low temperatures, corresponding to the [001] and [110] magnetic ordering wave vectors at 0.77 and 1.09 Å^{-1}, respectively, and the [111] nuclear structure wave vector at 1.32 Å^{-1}. The magnetic reflections are those expected for the type-I AFM structure [Fig. 1(a)] previously reported for this material [10,11], and fade away above $T_{N1} = 32$ K, as expected. In the inelastic sector, a dispersion band emerging from [001] is observed at low temperatures [see Figs. 1(b) and 1(c)]. Above T_{N2}, the excitation spectrum is dominated by a diffusive quasielastic column above the [001] magnetic wave vector, which persists up to at least 100 K [see Figs. 1(e)–

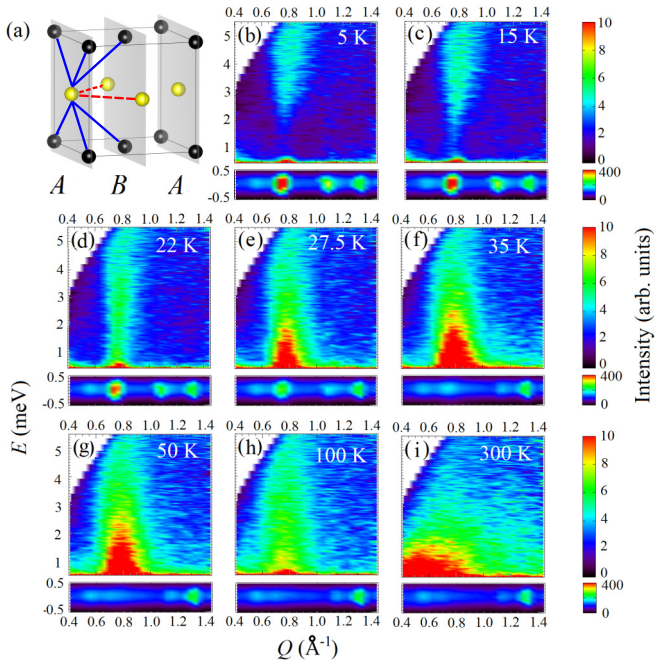

FIG. 1. (a) Type-I magnetic structure of Sr_2YRuO_6 below $T_{N2} =$ 24 K, where only Ru^{5+} magnetic ions are represented. Spheres of different colors represent opposite spins. The structure may be viewed as a stacking of square AFM layers in the $ABAB$ sequence. Satisfied (frustrated) AFM interactions between a selected Ru ion and its neighbors are shown as solid blue (dashed red) lines. (b)–(i) Inelastic neutron scattering intensity plots as a function of the wave vector and excitation energy for Sr_2YRuO_6 at (b) 5, (c) 15, (d) 22, (e) 27.5, (f) 35, (g) 50, (h) 100, and (i) 300 K, obtained with incident neutron energy $E_i = 9.73$ meV. The elastic signal is displayed separately on the bottom of each figure, corresponding to (from left to right) the magnetic [001], [110], and nuclear [111] reflections, respectively.

1(h)]. The spectrum at 300 K becomes much broader in Q [see Fig. 1(h)], as expected for a system evolving towards the uncorrelated paramagnetic state on warming.

Measurements with finer energy resolution using $E_i =$ 4.64 meV allow for a closer look at the quasielastic scattering in the fully ordered and correlated phases. Figures 2(a) and 2(b) show neutron scattering intensity plots as a function of

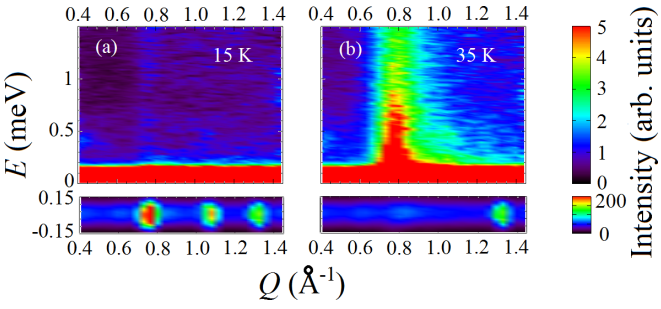

FIG. 2. Inelastic neutron scattering intensity plots as a function of the wave vector and excitation energy for Sr_2YRuO_6 at (a) 15 and (b) 35 K, obtained with $E_i = 4.64$ meV. The elastic signal is displayed separately on the bottom of each figure.

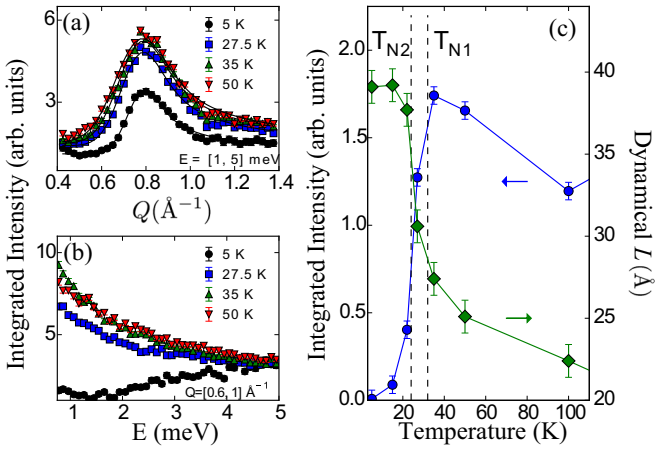

FIG. 3. (a) Energy-integrated scattering intensity at selected temperatures for $E = [1,5]$ meV, using data taken with neutrons with incident energy $E_i = 9.73$ meV. Solid lines are fits to scattering from two-dimensional layers according to the Warren model [31]. (b) Energy dependence of the neutron scattering intensity integrated in the wave-vector interval $Q = [0.6,1]$ Å^{-1} at selected temperatures. (c) Intensity integrated over the range $Q = [0.4,1.4]$ and $E = [1,2]$ (green diamonds) as a function of temperature. The sharp drop below T_{N1} corresponds to the opening of the spin gap. The blue circles denote the dynamical correlation length obtained from the Warren line-shape fits in (a) as a function of temperature. Error bars represent one standard deviation from either counting statistics or least-squares fits.

the wave vector and excitation energy of SYRO at 15 and 35 K, respectively. With this finer resolution it is apparent that the scattering is greatly suppressed between 0.2 and 1.5 meV in the ordered state, demonstrating that the spin waves are gapped below T_{N2}. In comparison, the diffusive quasielastic scattering at 35 K is rather strong, increasing with decreasing energy down to the experimental limit of 0.15 meV, as expected for correlated paramagnetism.

Figure 3(a) shows the Q dependence of the inelastic scattering integrated between 1 and 5 meV (denoted as $E =$ [1,5] meV) at selected temperatures. Although the inelastic scattering maps at 5 K and above 27.5 K are entirely different [see Figs. 1(b) and 1(e)–1(g)], their Q dependence is rather similar, with a broad asymmetric maximum at $Q = 0.77$ Å^{-1} corresponding to the [001] wave vector, while no relevant contribution centered at $Q = 1.09$ Å^{-1} corresponding to the [110] position is observed. This asymmetric line shape is characteristic of two-dimensional (2D) behavior, similar to that reported in our previous energy-integrated measurements [11]. We performed fits of these inelastic profiles with the Warren model for scattering from uncoupled layers [31], shown as the solid lines in Fig. 3(a), resulting in the effective dynamical correlation length as a function of temperature in Fig. 3(c). The correlation length first increases gradually with decreasing temperatures, then dramatically increases between T_{N2} and T_{N1} with the onset of magnetic order and well-defined spin-wave scattering. The integrated inelastic scattering below T_{N2} is also described by a Warren line shape, demonstrating a slight anisotropy of the powder-averaged direction, and that there is no stiffening of the spin-wave modes with decreased temperature.

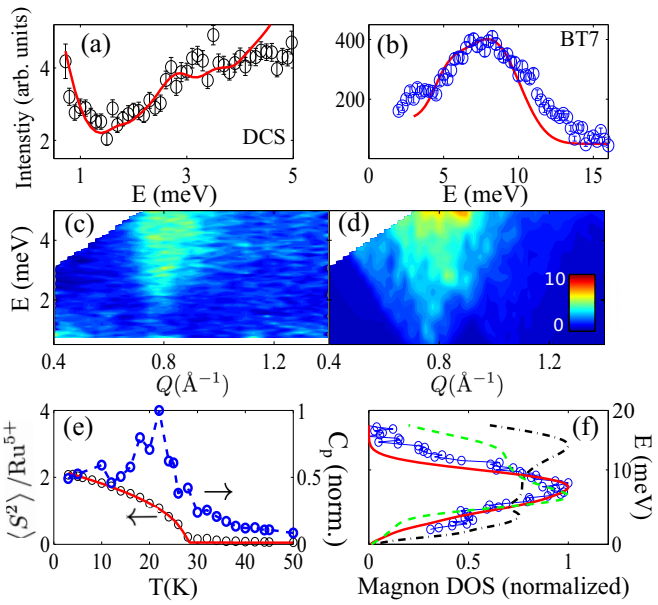

FIG. 4. (a) Energy-dependent intensity integrated over $Q = [0.6,1]$ Å^{-1} from Fig. 1(b). (b) Background-subtracted intensity centered at $Q = 1.3$ Å^{-1} measured on BT-7. The solid (red) lines in (a) and (b) correspond to best-fit set of parameters described in the text. (c) Measured and (d) calculated DCS spectra from these best-fit parameters. (e) Thermally averaged ordered moment and specific heat from Monte Carlo simulations showing $T_{N,\mathrm{calc}} = 27.5$ K. (f) Normalized magnon density of states for the best-fit model (solid red), model with third NN model [26] (dashed, green), and the anistropic exchange parameters with $J_1 = 15$ meV [12,14] model (dotted black). Normalized data from (b) are shown as open circles for comparison.

Further details on the spectral weight transfer with temperature are given by the energy dependence of the intensity integrated between $Q = 0.6$ and 1.0 Å^{-1} ($Q = [0.6,1]$ Å^{-1}), covering the scattering around the [001] magnetic ordering wave vector. This is shown in Fig. 3(b) for selected temperatures. At $E \sim 5$ meV, the scattering intensity is independent of temperature before accounting for thermal factors. Below this energy, the scattering at 5 K is strongly suppressed when compared to the signal at higher temperatures, corresponding to the opening of the spin gap. The temperature dependence of the correlations and onset of the spin gap is quantified by integrating the low-energy portion of the scattering, $E = [1,2]$ meV, shown in Fig. 3(c). The low-energy intensity increases with decreasing temperature down to T_{N1}, following the quasielastic scattering in Fig. 1. The sudden loss of intensity below T_{N1} demonstrates that the spin gap forms concomitantly with long-range order [11], similar to BYRO [26].

The top of the magnetic scattering band extends beyond the 5 meV maximum energy transfer shown here. Subsequent inelastic measurements were made on the BT-7 triple-axis spectrometer with energy transfers up to 16 meV at a constant $Q = 1.3$ Å^{-1}, the lowest allowable momentum transfer for energy in this configuration with sufficient resolution. The difference between 3 and 300 K data is shown in Fig. 4(b), after correcting for the Boltzmann temperature dependence, to separate the contribution from the spin-wave scattering. The rather sharp maximum at $E \sim 8$ meV signifies the maximum in the magnon density of states (DOS). This is similar to the energy-dependent scattering found in BYRO [25], with a 5 meV spin gap and 14 meV maximum in the DOS.

The magnetic structure below T_{N2} is well defined as a type-I AFM and thus the excitations may be modeled using spin-wave theory to first approximation. We employ the simplified Hamiltonian shown in Eq. (1) considering only nearest-neighbor (NN) interactions J_1, next-nearest-neighbor (NNN) J_2, and single-ion anisotropy D, with $S = \frac{3}{2}$ moments on the fcc lattice. The sign of the J_2 interactions and D are fixed to ensure a type-I ground state with spins lying in the plane, as previously observed [11],

$$H = \sum J_{ij} \vec{S}_i \vec{S}_j + D \sum \left(S_i^z\right)^2. \qquad (1)$$

The spin-wave excitations were calculated and powder averaged within linear spin-wave theory using the SPIN-W package [32]. The magnetic form factor for Ru^{5+} is not tabulated in standard tables and so the form determined in Ref. [33] was used for calculations and comparison with experiment. The interaction terms in Eq. (1) were determined by least-squares fitting the wave-vector-integrated and resolution-corrected magnetic scattering simultaneously to both the BT7 and DCS data shown in Figs. 4(a) and 4(b).

A constant background and overall scaling term were also included in each data set while a Gaussian of fixed amplitude and width was used to account for the elastic contribution. The resulting best fit is shown as the solid lines in Figs. 4(a) and 4(b), corresponding to $J_1 = 0.55(5)$ meV, $J_2 = -0.40(5)$ meV, and $D = 0.10(3)$ meV, and an excellent goodness of fit $\chi^2 = 1.6$. Calculation of the scattering intensity as a function of wave vector and energy reproduced the DCS data quite well, as in Fig. 4(b). The apparent lack of inelastic scattering above the [110] wave vector in Fig. 1(b), for example, can be conclusively attributed simply to the effect of powder averaging and rapidly vanishing form factor [33] which strongly suppress the observed scattering at this position, as suggested previously [25].

The onset of long-range magnetic order is well described within mean-field theory by this set of exchange parameters, as demonstrated by Monte Carlo calculations shown in Fig. 4(e). Using a grid of 14^3 unit cells (10 976 spins) the static magnetic moment is found to follow order-parameter-like behavior when a simulated annealing routine is performed, resulting in a single transition in both magnetization and specific heat with $T_N = 27.5$ K, quite close to that actually observed [11]. Furthermore, if we simply increase the magnitude of J_1 to 0.75 meV, we obtain a maximum in the spin-wave spectrum of 15 meV and $T_N = 38$ K, both quite close to that found in BYRO [25]. It should be noted that only one transition is possible with this mean-field analysis and simple model, and it therefore cannot capture the second transition or low-dimensional correlations at high temperatures. However, despite the simplicity of the J_1-J_2 model, it appears to capture many salient features correctly at the mean-field level, including the magnitude of the exchange interactions between Ru ions.

Previous *ab initio* and Mössbauer studies have suggested J_1 on the order of 15–20 meV, with symmetric exchange

anisotropy resulting in a lower magnetic ordering temperature [8,12,14]. However, as shown in Fig. 4(f), the integrated magnon density of states (DOS) for this model with no single-ion anisotropy and $J_2/J_1 = -0.01$ does not result in a single well-defined peak in this energy range, but rather global maxima at energies well above 100 meV. An additional model incorporating all AFM exchange interactions up to third nearest neighbor with fixed proportions recently suggested for BYRO [26] was also examined. This resulted in a best-fit $J_1 =$ 1.5 meV, on the same order of magnitude as the simple J_1-J_2 model, but did not produce a single maximum in the DOS, as the J_3 interactions break the degeneracy of the spin-wave modes at higher energies. Other models incorporating different types of further-neighbor interactions or other anisotropies such as the Dzyaloshinskii-Moriya interaction could not be reliably studied due to the polycrystalline averaging.

The suppression of inelastic scattering below T_{N1} corroborates recent results that spin-orbit coupling (SOC) is the primary source of single-ion anisotropy in these systems [25,28,34], leading to the observed gap in the spin-wave spectrum. This anisotropy favors ferromagnetic alignment of the spins within the a-b plane and alternating along the c axis as determined from previous high-resolution powder diffraction measurements [11]. As a result, the spin gap is nonuniform between zone centers, similar to other single domain type-I AFM structures [35]. Calculations of the full spin-wave dispersion using our best-fit exchange constants reveal a spin gap of roughly 2 meV at [00q]-type reciprocal lattice vectors and 0.5 meV for [qq0] type, resulting in the very weak scattering below 2 meV in the powder-averaged scattering spectra in Figs. 4(a) and 4(b) and in Fig. 2(a) to a lesser extent. In addition to SOC, distortions of the oxygen octahedra around each Ru ion may also act to break the degeneracy of the t_{2g} and e_g manifolds and subsequent Ru-O bonding, which will in turn effect the relative strength of the superexchange pathways [14]. In fact, recent systematic studies of Ca-doped SYRO [36] have found T_{N1} does in fact decrease monotonically with increasing monoclinic distortion, in agreement with our results here. If such distortions instead generated anisotropy in the exchange interaction matrix, one would expect frustration to be relieved and an increased T_N [8], which is not observed.

Both the shape of the quasielastic spectra and spectral weight transfer from excitations on cooling [see Fig. 3(d)] provide important insight into the mechanism of the long-range ordering transition and correlated scattering. The column of quasielastic excitations observed above the [001] wave vector at intermediate temperatures is characteristic of a dense population of quasistatic correlated layers. The lowest-energy excitations in this state are arguably related to cluster size fluctuations between planes. At sufficiently low temperatures, correlated two-dimensional clusters merge and condense, while the signal from size fluctuations is suppressed, giving rise to elastic Bragg scattering. A similar mechanism was recently proposed to explain the diffuse scattering above T_{N1} in BYRO [26], but suggested the primary correlations are quasi-one-dimensional rather than 2D, as we have shown here.

In summary, the magnetic excitations of Sr_2YRuO_6 were investigated by inelastic neutron scattering. The spin dynamics in the ordered state are adequately described within linear spin-wave theory with exchange interaction energies far smaller than early predictions. Observation of significant correlations at temperatures an order of magnitude higher than T_{N1}, with asymmetric linewidths, is indicative of strong 2D correlations, demonstrating low-dimensional spin correlations for all temperatures above T_{N2}. Similarities with cubic BYRO demonstrate a common exchange-interaction model among double-perovksite ruthenates, regardless of crystallographic distortions, in which SOC may play an important role in establishing the magnetically ordered state in these frustrated fcc antiferromagnets.

This work was supported in part by FAPESP Grants No. 2012/04870-7, 2013/07296-2 and No. 2014/19245-6 and CNPq, Brazil, and NSF Grant No. DMR-0805335, USA.

[1] C. Lacroix, P. Mendels, and F. Mila, *Introduction to Frustrated Magnetism* (Springer, Berlin, 2011).
[2] P. W. Anderson, Phys. Rev. **79**, 705 (1950).
[3] M. E. Lines, Phys. Rev. **139**, A1304 (1965).
[4] Y.-Y. Li, Phys. Rev. **84**, 721 (1951).
[5] S. Vasala and M. Karppinen, Prog. Solid State Chem. **43**, 1 (2015).
[6] S.-H. Lee, H. Takagi, D. Louca, M. Matsuda, S. Ji, H. Ueda, Y. Ueda, T. Katsufuji, J.-H. Chung, S. Park, S.-W. Cheong, and C. Broholm, J. Phys. Soc. Jpn. **79**, 011004 (2010).
[7] D. D. Cox, IEEE Trans. Magn. **8**, 161 (1972).
[8] E. V. Kuz'min, S. Ovchinnikov, and D. Singh, JETP **96**, 1124 (2003).
[9] E. V. Kuz'min, S. G. Ovchinnikov, and D. J. Singh, Phys. Rev. B **68**, 024409 (2003).
[10] P. Battle and W. Machlin, J. Solid State Chem. **52**, 138 (1984).
[11] E. Granado, J. W. Lynn, R. F. Jardim, and M. S. Torikachvili, Phys. Rev. Lett. **110**, 017202 (2013).
[12] G. Long, M. DeMarco, D. Coffey, M. K. Toth, and M. S. Torikachvili, Phys. Rev. B **87**, 024416 (2013).
[13] G. Cao, Y. Xin, C. S. Alexander, and J. E. Crow, Phys. Rev. B **63**, 184432 (2001).
[14] R. P. Singh and C. V. Tomy, Phys. Rev. B **78**, 024432 (2008).
[15] P. L. Bernardo, L. Guivelder, G. G. Eslava, H. S. Amorim, E. H. C. Sinnecker, I. Felner, J. J. Neumeier, and S. García, J. Phys.: Condens. Matter **24**, 486001 (2012).
[16] S. Garcia and L. Guivelder, Solid State Commun. **179**, 11 (2014).
[17] L. O.-S. Martin, J. P. Chapman, L. Lezama, J. S. Marcos, J. Rodriguez-Fernandez, M. I. Arriortua, and T. Rojo, Eur. J. Inorg. Chem. **2006**, 1362 (2006).
[18] A. Munoz, J. A. Alonso, M. T. Casais, M. J. Martinez-Lope, and M. T. Fernandez-Diaz, J. Phys.: Condens. Matter **14**, 3285 (2002).
[19] A. A. Aczel, D. E. Bugaris, J. Yeon, C. de la Cruz, H.-C. zur Loye, and S. E. Nagler, Phys. Rev. B **88**, 014413 (2013).
[20] J.-W. G. Bos and J. P. Attfield, Phys. Rev. B **70**, 174434 (2004).

[21] P. D. Battle, C. P. Grey, M. Heriveu, C. Martin, C. A. Moore, and Y. Paik, J. Solid State Chem. **175**, 20 (2003).
[22] A. García-Flores, H. Terashita, E. Bittar, R. F. Jardim, and E. Granado, J. Raman Spectrosc. **45**, 193 (2014).
[23] P. L. Bernardo, L. Ghivelder, H. S. Amorim, J. J. Neumeier, and S. García, New J. Phys. **17**, 103007 (2015).
[24] P. D. Battle and C. W. Jones, J. Solid State Chem. **78**, 108 (1989).
[25] J. P. Carlo, J. P. Clancy, K. Fritsch, C. A. Marjerrison, G. E. Granroth, J. E. Greedan, H. A. Dabkowska, and B. D. Gaulin, Phys. Rev. B **88**, 024418 (2013).
[26] G. J. Nilsen, C. M. Thompson, G. Ehlers, C. A. Marjerrison, and J. E. Greedan, Phys. Rev. B **91**, 054415 (2015).
[27] A. A. Aczel, D. E. Bugaris, L. Li, J.-Q. Yan, C. de la Cruz, H.-C. zur Loye, and S. E. Nagler, Phys. Rev. B **87**, 014435 (2013).
[28] A. A. Aczel, P. J. Baker, D. E. Bugaris, J. Yeon, H.-C. zur Loye, T. Guidi, and D. T. Adroja, Phys. Rev. Lett. **112**, 117603 (2014).
[29] T. Aharen, J. E. Greedan, C. A. Bridges, A. A. Aczel, J. Rodriguez, G. MacDougall, G. M. Luke, V. K. Michaelis, S. Kroeker, C. R. Wiebe, H. Zhou, and L. M. D. Cranswick, Phys. Rev. B **81**, 064436 (2010).
[30] J. W. Lynn, Y. Chen, S. Chang, Y. Zhao, S. Chi, W. Ratcliff, II, B. G. Ueland, and R. W. Erwin, J. Res. Natl. Inst. Stand. Technol. **117**, 61 (2012).
[31] B. Warren, Phys. Rev. **59**, 693 (1941).
[32] S. Toth and B. Lake, J. Phys.: Condens. Matter **27**, 166002 (2015).
[33] N. G. Parkinson, P. D. Hatton, J. A. K. Howard, C. Ritter, F. Z. Chiend, and M.-K. Wu, J. Mater. Chem. **13**, 1468 (2003).
[34] E. Kermarrec, C. A. Marjerrison, C. M. Thompson, D. D. Maharaj, K. Levin, S. Kroeker, G. E. Granroth, R. Flacau, Z. Yamani, J. E. Greedan, and B. D. Gaulin, Phys. Rev. B **91**, 075133 (2015).
[35] B. Hälg and A. Furrer, Phys. Rev. B **34**, 6258 (1986).
[36] P. Bernardo, L. Ghivelder, G. Eslava, H. Amorim, I. Felner, and S. Garcia, J. Solid State Chem. **220**, 270 (2014).